43rd AIAA Aerospace Sciences Meeting and Exhibit
10 - 13 January 2005, Reno, Nevada

AIAA 2005-1000

Progress in Validation of Wind-US for Ramjet/Scramjet Combustion

William A. Engblom[1]
The Aerospace Corporation, Cleveland, Ohio

Franco C. Frate[2]
QSS Group, Inc., Cleveland, Ohio

and

Chris C. Nelson[3]
Innovative Technology Applications Company, LLC, Seattle, WA

Validation of the Wind-US flow solver against two sets of experimental data involving high-speed combustion is attempted. First, the well-known Burrows-Kurkov supersonic hydrogen-air combustion test case is simulated, and the sensitivity of ignition location and combustion performance to key parameters is explored. Second, a numerical model is developed for simulation of an X-43B candidate, full-scale, JP-7-fueled, internal flowpath operating in ramjet mode. Numerical results using an ethylene-air chemical kinetics model are directly compared against previously existing pressure-distribution data along the entire flowpath, obtained in direct-connect testing conducted at NASA Langley Research Center. Comparison to derived quantities such as burn efficiency and thermal throat location are also made. Reasonable to excellent agreement with experimental data is demonstrated for key parameters in both simulation efforts. Additional Wind-US features needed to improve simulation efforts are described herein, including maintaining stagnation conditions at inflow boundaries for multi-species flow. An open issue regarding the sensitivity of isolator unstart to key model parameters is briefly discussed.

I. Nomenclature

c	=	speed of sound
C_f, C_b	=	forward and backward reaction rate coefficients
D_f, D_b	=	forward and backward reaction activation energies
K_B	=	Boltzmann constant
L	=	length of test section
MW	=	molecular weight
P	=	static pressure
P_{max}	=	maximum pressure along test section
P_o	=	stagnation pressure
R	=	Molar gas constant
R_2	=	Reimann invariant
S_f, S_b	=	forward and backward reaction rate exponent
T	=	static temperature
$F_{x,ratio}$	=	ratio of numerical-to-experimental axial thrust
T_o	=	stagnation temperature
u	=	axial velocity
V	=	total velocity magnitude
x	=	axial position

[1] Engineering Specialist, Fluid Mechanics, 21000 Brookpark Rd, Mail 86-7, AIAA Senior Member.
[2] Research Engineer, Inlet Branch, 21000 Brookpark Rd, Mail 86-7, AIAA Member.
[3] Senior Scientist, 6712 183rd St SW, Lynnwood WA 98037, AIAA Senior Member.

k = turbulent kinetic energy
$\eta_{\text{burn, ratio}}$ = ratio of numerical-to-experimental burn efficiency
ε = turbulent dissipation
ϕ = equivalence ratio
γ = ratio of specific heats
φ = angle of velocity vector relative to grid normal
Pr_t = turbulent Prandtl number

II. Introduction

There is currently national interest in development of high-speed propulsion systems (e.g., ramjet/scramjet combined cycle) at NASA (e.g. X-43) and the DoD (e.g. HyFly). The recent successful flights of the X-43A have bolstered this enthusiasm within the NASA community. Consequently, there is interest in development and evaluation of numerical modeling tools to supplement relatively expensive ground testing. Validation of such tools against realistic full-scale engine tests is clearly necessary to establish confidence in the numerical modeling approach.

The Wind flow solver (predecessor to Wind-US) has been utilized to predict and evaluate the performance of high-speed air breathing engine components, including inlets and isolators [1,2], and nozzles [3] in support of the X-43B-related Integrated System Test of an Airbreathing Rocket (ISTAR) program, but have excluded combustor components. Over the past few years the NPARC Alliance, a partnership between the USAF (Arnold Engineering Development Center), NASA (Glenn Research Center), and The Boeing Company (Phantom Works in St. Louis), has invested significant resources towards refinement and validation of Wind, and more recently Wind-US, for chemically reacting flows [4-7]. Consequently, it is now more appropriate to consider utilizing Wind-US to simulate an entire internal flowpath, which is the focus of the current paper. We suggest that the common practice of decoupling analyses of engine components can lead to significant prediction uncertainties that would be mitigated via fully-coupled flowpath simulation. With the recent addition of an unstructured grid capability to the already present structured grid capabilities (e.g. abutting or overlapping blocks), Wind-US also offers tremendous grid generation flexibility when dealing with complex full-scale vehicle configurations, making internal/external tip-to-tail simulation more practical.

We attempt to validate the Wind-US, version 1, structured flow solver against full-scale engine data (and analytically derived performance metrics) for a test article derived from a candidate X-43B configuration. This experimental data set [8] is from "direct-connect" engine tests conducted using the Injector Characterization Rig (ICR) at NASA Langley by the RBCC Consortium (RBC^3) in the summer/fall of 2003.

III. Methodology

Before attempting to simulate the ICR experiment, we first examine a benchmark case of the Burrows-Kurkov hydrogen-air supersonic combustion experiment [9] with Wind-US. Although there have been three documented attempts [6,7,10] to simulate this experiment with predecessors of Wind-US, these efforts have shown varied success compared to the published results by Ebrahimi [11] using other flow solvers. Also, Wind-US Version 1.0 is still a relatively new version that has undergone extensive modification, including conversion to entirely Fortran 90. So, we felt this exercise was necessary to re-validate the solver.

Next, we attempt to simulate the JP-7/air Mach 2 experiment run on the full-scale partial section of the X-43B flight engine. We decided to simulate a specific ram mode run (i.e. Run 112) that is well-documented and includes all three types of injectors in the experiment (i.e., cascade, base, and ram).

Chemical Reaction Models

Based on experience with the GASP solver [12], it was expected that the Burrows-Kurkov simulation results would improve (i.e., peak H_2O mole fraction levels are better captured) when the standard H_2-air model from Evan and Schexnayder [13] was modified to include third-body efficiencies (other than unity) from the Jachimowski model [14]. In fact, peak combustor exit temperatures and product mole fraction levels are increased by about 20%. The resulting peaks match experimental measurements quite well (see Results section). Consequently, a new H_2-air

kinetics model was added to the Wind-US chemical kinetics database (see Table 1). Based on the success of other researchers with the Vulcan code at simulating aspects of hydrocarbon-air combustion in ramjets and scramjets [15,16], we choose to add and utilize the 7-species, 3-step ethylene-air kinetics model from Mawid [17] to the Wind-US chemical kinetics database (see Table 2). We conducted simulations of the 3-D ramjet engine test with this 3-step model from Mawid and with the 5-species, 1-global step, ethylene-air model from Westbrook and Dryer [18] already available in Wind-US.

Table 1: Modified Evan and Schexnayder H_2-Air Mechanism
8 Reactions, 7 species: O2, H, H_2, H_2O, OH, O, N_2

Reaction	S_f S_b	D_f/K_B D_b/K_B (K)	C_f C_b (cm^3/mole-sec)
$O_2 + (M) = O + O + (M)$ third body efficiency H_2 2.5, H_2O 16.25 1.0 for all others	-1.0 -1.0	5.9340E+04 0.0	7.20E+18 4.00E+17
$H_2 + (M) = H + H + (M)$ third body efficiency H_2 2.5, H_2O 16.25 1.0 for all others	-1.0 -1.0	5.1987E+04 0.0	5.50E+18 1.80E+18
$H_2O + (M) = OH + H + (M)$ third body efficiency H_2 2.5, H_2O 16.25 1.0 for all others	-1.5 -1.5	5.9386E+04 0.0	5.20E+21 4.40E+20
$OH + (M) = O + H + (M)$ third body efficiency H_2 2.5, H_2O 16.25 1.0 for all others	-1.0 -1.0	5.0830E+04 0.0	8.50E+18 7.10E+18
$O_2 + H = OH + O$	0.0 0.0	8.4550E+03 0.0	2.20E+14 1.50E+13
$H_2 + O = OH + H$	0.0 0.0	5.5860E+03 4.4290E+03	7.50E+13 3.00E+13
$H_2O + O = OH + OH$	0.0 0.0	9.0590E+03 5.0300E+02	5.80E+13 5.30E+12
$H_2O + H = OH + H_2$	0.0 0.0	1.0116E+04 2.6000E+03	8.40E+13 2.00E+13

Table 2: Mawid 3-Step Ethylene/Air Mechanism
3 Reactions, 7 species: C_2H_4, O_2, CO_2, H_2O, N_2, H_2, CO

Reaction	S_f	D_f/K_B (K)	C_f (cm^3/mole-sec)
$2\ CO + O_2 = 2\ CO_2$	X	X	X
$2\ H_2 + O_2 = 2\ H_2O$	X	X	X
$C_2H_4 + O_2 = 2\ CO + 2\ H_2$	X	X	X

Note: Reaction rate parameters suppressed by request of Mawid [17]

Stagnation Boundary Condition for Multi-Species Simulations

Previous versions of Wind did not permit fixed stagnation conditions at a boundary for multi-species runs. This limitation has now been removed by the addition of a new "hold totals" inflow boundary condition for multi-species flows. This boundary condition starts by stating that we wish to hold constant some approximation to the total temperature and total pressure, as well as the direction of the velocity vector (but not its magnitude) and species mole fractions. Within those constraints, all other properties can vary. For supersonic inflow, of course, all

variables may be specified and the application of the boundary condition is, therefore, straightforward. For subsonic inflow, however, one piece of information is required from the interior of the flow. In this case, we have chosen to extrapolate the outgoing Riemann invariant:

$$R_2 = \frac{V}{\sqrt{\tan^2\varphi + 1}} - \frac{2c}{\gamma - 1} \tag{1}$$

Where V is the flow velocity at the boundary and φ is the flow angle (relative to the normal vector) at the boundary. The speed of sound, c, is given by:

$$c = \sqrt{\gamma R T} \tag{2}$$

Where T is the temperature of the mixture, and γ and R are the ratio of specific heats and gas constant for the mixture at that temperature. The value for R_2 is determined using a first order extrapolation from the two nearest interior points.

There are several possible definitions that could be used for "total temperature" in a reacting flow. For the purposes of this boundary condition, the "total temperature" is defined by the isentropic relation:

$$T_0 = T\left(1 + \frac{\gamma - 1}{2}\left(\frac{V}{c}\right)^2\right) \tag{3}$$

Using this, the equation for the speed of sound, and the definition of the Riemann invariant, one can construct the following quadratic equation:

$$\left[\left(\tan^2\varphi + 1\right)\frac{(\gamma - 1)R_2^2}{2\gamma R} - T_0\right] + \frac{2\left(\tan^2\varphi + 1\right)R_2}{\sqrt{\gamma R}}\tau + \left[\frac{2\left(\tan^2\varphi + 1\right)}{\gamma - 1} + 1\right]\tau^2 = 0 \tag{4}$$

where $\tau \equiv \sqrt{T}$

Since T must always be positive and the flow angle, φ, must always be such that flow is entering the domain through the inflow boundary, the above quadratic must have a real root, which is easily obtained. Unfortunately, unlike with perfect gases, the ratio of specific heats is a function of temperature. Therefore, associated with the new temperature, a new value for γ must be computed, and the process iterates until the desired level of convergence is reached. Because of intermittent stability problems experienced with Newton iterations, a Jacobi iteration method has been used here with a convergence tolerance on the relative error of 10^{-7}. Once final values of T and γ have been reached, the remaining flow quantities can be determined in a straightforward fashion. The speed of sound is known from the relation given above. The velocity magnitude is given by the following equation derived from the definition of the Riemann invariant:

$$V = \left(R_2 + \frac{2c}{\gamma - 1}\right)\sqrt{\tan^2\varphi + 1} \tag{5}$$

The specific components can be computed based on the specified flow direction. The pressure at the boundary is now computed from the isentropic relationship (thus defining the “total pressure” that is being held) as:

$$P = P_0\left(1+\frac{\gamma-1}{2}\left(\frac{V}{c}\right)^2\right)^{\frac{-\gamma}{\gamma-1}} \tag{6}$$

Now the density may be computed using the equation of state:

$$\rho = \frac{P}{RT} \tag{7}$$

At this point, enough information is available to compute the entire boundary state, and the algorithm is complete.

Model Description for 2-D Hydrogen-Air Combustion Simulation

A schematic for the Burrows-Kurkov experiment is provided in Fig. 1. The inflow consists of hot (T=2286 R) vitiated air at Mach 2.44 in the main stream, with cold (T=400 R), pure hydrogen injected at sonic speed. The grid used for the Burrows-Kurkov test case consisted of a 121x 145 (35.6 cm long) for the test section. For some runs an additional 81 x 81 grid (42 cm long) to develop a boundary layer similar to that described in [9]. The sensitivity of ignition location and combustor exit profiles to the choice of turbulence model, *Prt*, and inflow profile (i.e. developed numerically prior to test section, or imposed using experimental data) is examined.

Model Description for 3-D Hydrocarbon-Air Ramjet Simulation

A schematic for the Injector Characterization Rig (ICR) test engine is provided in Fig. 2. The overall grid is composed of roughly 8 million cells within 49 blocks, some with mismatched boundaries to control grid resolution. All geometric details of the test article are preserved. For example, the internal contours of the complex cascade injector was digitized and modeled exactly. The injectors are also positioned as in the experiment. The nearfield of each injector is well-resolved to avoid too much numerical dissipation, and potential over-mixing of the fuel stream with the main airflow. For example, the nearfield of the cascade injector contains roughly 1 million cells. It is not clear whether this resolution was sufficient (or overkill) since no grid independence study was conducted. The computations were typically conducted with one level of grid sequencing (i.e., every other grid point in each coordinate direction is dropped), due to the severe CPU time requirements imposed by the fine grid. The grid spacing along the wall resulted in y+ values of typically less than 1. The parallel decomposition was chosen for greater than 90% efficiency on 24-processors.

Since the experiment was conducted using JP-7 fuel, and we wish to use an ethylene-air chemical kinetics model, modifications to the numerical model geometry were necessary to maintain the same chemical energy rate as the experiment. Recall the definition of chemical energy rate:

$$\text{Chemical energy rate} = \text{mass flow rate of fuel} * \text{heat of reaction} \tag{8}$$

Mass flow thru a sonic or supersonic injector is proportional to $\sqrt{MW}$. So, in order to match the fuel mass flow rate of gaseous JP-7 ($C_{12}H_{25}$; MW = 169.0 [19]) with ethylene (C_2H_4; MW = 28.0), assuming the same $\gamma(T)$, and holding reservoir stagnation condition constant, we must increase the throat area by 2.46, which corresponds to a scale-up of the injector size of 1.57 in each direction. Consequently, the numerical injectors are made 57% larger in diameter than the experimental injectors, to maintain the same mass flow rate of fuel, while maintaining their centerline positions.

Fortunately the fuel heat of reaction is not significantly different between the numerical model and experiment. It is assumed that the JP-7 in the experiment was pure, superheated gas that is uncracked (i.e., contains large hydrocarbon chains), based on available thermodynamic information [8]. Since the heat of reaction for JP-7 is 18,700 Btu/lbm [19] and ethylene is 20,200 Btu/lbm, the endothermic pyrolytic reactions that crack JP-7 into small hydrocarbon chains into pure ethylene requires about 1,500 Btu/lbm. Consequently, we should reduce the fuel rate by 7% to retain the same chemical energy rate.

We conclude that the injectors should be scaled-up by 50% (57% - 7%) compared to experiment to retain the chemical energy rate. We elected to keep the aforementioned 57% injector scale-up estimate and then slightly adjust the fuel flow rate downward via the reservoir stagnation pressure. As expected, we were able to get an equivalence ratio for ethylene-air very similar to that for JP-7 in the experiment.

The numerical scheme was configured based on previous experiences with the Wind solver. Menter's Shear Stress Transport (SST) turbulence model was chosen for these computations, along with Wind-US default values for Pr_t (i.e. 0.9) and Sc_t (i.e. 0.9). The sensitivity to turbulence model parameters was not addressed for this simulation. Roe's 2nd order upwind scheme was chosen for the inviscid flux function, with default compression to enforce the TVD property. The default implicit time advancement scheme (i.e. spatially-split approximate factorization) with local time stepping and a CFL of 0.1-0.2 was chosen to drive the solution towards steady-state. In general the solutions did not become fully steady-state, but rather pseudo-steady due primarily to oscillations within the flame holder (step combustor) region. It was also necessary to reduce the activation energy by 50% for several hundred cycles to ignite and develop a flame, followed by thousands of cycles of simulation at the standard activation levels.

IV. Results

2-D Hydrogen-Air Supersonic Combustion Simulation

Fig. 3 illustrates the sensitivity of the predicted ignition location and flame extent for the Burrows Kurkov simulation to turbulence model and turbulent Prandtl number. For these runs, the boundary layer is developed numerically along a uniform duct extension length of 42 cm, starting from uniform flow. The length was found to produce a kinematic boundary layer height at the step (at x = 0) similar to that measured in the experiment (i.e., roughly 1 cm assuming u = 99% U_∞). The dashed black line indicates the axial location of ignition from the experiment to occur at x = 25 cm for this case of T_∞ = 1270 K (2280 R). The axial locations of ignition are somewhat upstream compared to experiment, between x=14 cm and 18 cm. In the experiment ignition was determined based on onset of ultraviolet radiation, while in the numerics we arbitrarily assume onset occurs where temperature reaches 4000 R (red contour).

The effect of turbulence model is significant since the mixing rate is a primary driver of ignition. The SST model leads to faster mixing, and thus ignition, than the k-ε because the latter uses the Sarkar compressibility correction to reduce mixing at high speed. The standard SST model was constructed for incompressible flows and has no such compressibility corrections. Evaluation of the compressible version of the SST model recently made available in Wind-US is left for a future exercise. The sensitivity results indicate that ignition moves very slightly downstream with decreasing Pr_t (i.e. increased turbulent thermal conductivity/diffusivity). This occurs because increased transport of freestream thermal energy leads to more heat loss along the walls leading up to the mixing region, and less thermal energy in the freestream air. This leads to a lower static temperature in the mixing region, and finally to reduced reaction rates, and delayed ignition.

Fig. 4 illustrates the same sensitivities of the predicted hydrogen-air ignition location and flame extent with different inflow conditions. For these runs, the boundary layer is imposed at the step using digitized u and T profiles from the experiment. Ebrahimi [11] demonstrated that the inflow boundary definition was crucial towards obtaining the correct combustor exit conditions. As expected, the ignition delay compares quite well with experiment, especially for the k-ε runs. We also set the inflow turbulence quantities (k and ε) to be consistent with an equilibrium turbulent boundary layer, following the procedure from Launder and Spalding [20], as suggested by Ebrahimi. The digitized kinematic and thermal boundary layer profiles are compared to the numerically developed boundary layer profiles in Fig. 5. Although the axial velocity profiles agree well, the baseline case of Pr_t = 0.9 results in a much smaller thermal boundary layer than in the experiment. Assuming a Pr_t = 0.5 improves this thermal boundary layer comparison slightly. The delay in ignition for these cases (Fig. 4) relative to the numerically developed boundary layer cases is attributed to this thicker thermal boundary layer. Apparently there is much more air heat loss in the experiment (e.g. along supply nozzle walls) than obtained along the straight duct run-up assumed in the numerics. Perhaps a more accurate representation of the experimental set-up prior to the test section would provide improved results.

Figs. 6 and 7 depict comparisons between the aforementioned numerical runs and the experiment results for combustor exit flow state. For the numerically developed boundary layer cases (Fig. 6), the agreement for each quantity, except Mach number, is improved for $Pr_t = 0.5$ versus $Pr_t = 0.9$, for both turbulence models. The effect of turbulence model is relatively modest here. The peak stagnation temperature and peak H_2O mole fraction combustion product agree very well with experiment. The distance from the wall for these peaks also agrees quite well for the $Pr_t = 0.5$ results. For the specified boundary-layer cases (Fig. 7), the differences between the solutions are subtler. Again, peak levels are accurately captured. However, the flame is clearly more thick and diffuse than the experimental data, based on the comparisons for stagnation temperature. Consequently, it would appear that the relatively thin flame results for the numerically developed boundary layer cases are a better representation. The results reinforce the idea that the inflow thermal boundary layer just prior to mixing/combustion has a pronounced effect on the accuracy of the numerical simulation.

Fig. 8 illustrates the sensitivity of ignition delay to the temperature of the vitiated airflow. The axial distance (or ignition delay) increases linearly as temperature decreases for the first three cases. It is not clear why the linear trend discontinues for the lowest temperature case. The experimental data shows the same linear relationship of ignition delay to air temperature. However, in the experiment, ignition is delayed 25 cm for a temperature drop of 100 R; while in the numerics, the ignition is delayed only 7 cm for the same temperature drop of 100 R. Since ignition delay (and resulting residence time) is a crucial element of scramjet performance prediction, this represents a significant deficiency in the model. It is not clear if the aforementioned thermal boundary layer deficiency affects the slope of the ignition delay versus air temperature. Investigation of more detailed chemical kinetics models and limiting chemical reaction rates via a mixing rate limitation (e.g., eddy dissipation concept) may provide an improved capability to predict ignition delay sensitivity to air temperature.

3-D Hydrocarbon-Air Subsonic Combustion Simulation

Initial attempts to simulate the full-scale test run from scratch, with either the 1-step or 3-step kinetics models, resulted in isolator inlet unstarts. We decided to try two different incremental approaches to setting the inflow conditions so as to avoid isolator unstart. Specifically, we tried to 1) incrementally decrease the inflow Mach number from 3.0 to the test condition of 2.0; and 2) incrementally increase the fuel reservoir stagnation pressures to the injectors from 50% to 100%. We hoped to obtain converged solutions (i.e., isolator shock train fixed) that are close to the actual test conditions, and determine at what point (and why) the isolator unstarts.

For the first approach, we found that a converged solution could be obtained for an incoming airflow Mach number as low as Mach 2.25, with an isolator shock train which oscillates slightly back-and-forth in axial position; but that at Mach 2.0 the isolator shock structure monotonically moves slowly upstream until reaching the inflow boundary (i.e. unstart). Note that there is significant unsteadiness in the low speed combustion region behind the step (i.e. within the step combustor), and so by converged, we really mean pseudo-steady.

Fig. 9a contains the axial pressure profile for the Mach 2.25 inflow result. This profile is based on extracted values from approximately the center of the duct along the entire flowpath. This profile is also ensemble-averaged from the last 100 realizations (taken every 250 iterations) to smooth out the unsteadiness, especially along the step combustor region. The experimental data is from static pressure taps along the duct path. At some axial stations there were more than one tap, and so more than one symbol appears at that axial station. Since the pressure profiles are more-or-less 1-D in the experiment and in the numerics (away from the injector plumes), we feel this is an appropriate comparison of pressure profiles. The pressure levels are clearly too large compared to experiment over the entire axial length, though the peak pressure is predicted fairly well. The excess pressure levels start from the step combustor to the nozzle exit, where the levels are as much as 35% too high. This significant overprediction is related to the higher stagnation pressure of the freestream air, despite the lower ϕ. Note that equivalence ratio decreases because air mass flow increases at higher Mach number with all other inflow boundary conditions fixed.

Fig 9b depicts the Mach number profile, again ensemble-averaged for the Mach 2.25 inflow result. The flow within the flame holder and initial nozzle regions are subsonic, but thermal-choke eventually occurs at x/L = 65%, compared to the experimental value of 58% (an analytical estimate from Ref. 8 obtained using the experimental pressure profile and the HyCAD program). This difference may be attributed to the lower ϕ in the numerics (due to increased air flow), which should result in less optimal combustion, lower flames temperatures, and slower heat release. However, thermal choke location is a complex function of temperature, temperature gradient, area and area gradient [21].

Fig. 10a illustrates zero axial velocity isosurfaces colored by static pressure. The reverse flow regions behind the step are expected. The slender reverse flow regions within the isolator are similar to those described in References [2] and [22]. This slender structure only appears in the corner near the cascade injectors and extends about half of the isolator length. Fig. 10b shows a crossflow cut of the axial velocity contours taken approximately thru the axial midpoint of this long structure. The latter shows counter-rotating vorticity via crossflow streamlines, and a strong upstream current. That is, flow is being pumped upstream. Unfortunately, it is not clear whether or not such a structure existed in the experiment. This structure originated near the step and extended forward as the simulation continued, with a normal shock attached at its most upstream end. For near-Mach 2 inflow, it is reasonable to expect either a normal shock train or an oblique shock train [21].

Fig. 11a contains an axial pressure profile for the Mach 2.0 inflow result. Clearly, the agreement is much better than for the Mach 2.25 condition. Some important statistics for this simulation are compared with experimental results (derived using the HyCAD analytical method in Ref. 8) are provided in Table 3. Note that this case was initialized from the Mach 2.25 result. The isolator shock structure, and slender reverse flow region in Fig. 10a, continued to move upstream until the upstream boundary (i.e. until unstart). Consequently, this is *not* an entirely converged result. This axial pressure profile is an ensemble-averaging of the last 100 realizations prior to unstart. The solution prediction downstream of the isolator became pseudo-steady well before unstart. Therefore, it is reasonable to expect that if the isolator were long enough, we may have contained the reverse flow region and obtained a converged result for the entire flow path. The pressure levels agree very well until the aft portion of the combusting nozzle except for near the nozzle exit. The total stream thrust (divided by the experimental value) at the diverging nozzle exit compares quite well (4% low). The burn efficiency (again, divided by the experimental value) at the nozzle exit is 15% less than in the experiment.

Table 3: Summary of Combustion Statistics (Wind-US vs. Experiment)

	Experiment (HyCAD-derived)	Wind-US
M (inflow)	2.0	2.0
ϕ	0.95	0.91
$\eta_{\text{burn, ratio}}$	1.00	0.85
x_{throat}	58%	60%
$F_{x,ratio}$	1.00	0.96

Fig. 11b shows the corresponding Mach number profile for the Mach 2.0 simulation. This time the thermal choke occurs at x/L = 60%, which is very close to the experimental estimate of 58%. This is another indication that the heat release is being simulated properly. So, it would appear that the underprediction of isolator performance is the only significant disagreement between the numerics and experiment.

As stated earlier, for the second approach, we incrementally increase the fuel reservoir stagnation pressure (i.e., increase fuel mass flow rate), starting from 50% of the experimental fuel rates (i.e. 50% of the stagnation pressure supplied to the fuel injectors). In this approach we also choose to use the 1-step Westbrook and Dryer model. The 75% case re-initialized from the converged 50% case eventually led to unstart (shock train/separation moving upstream to the inflow boundary). Fig. 12a shows the converged axial pressure profile that resulted from the 50% fuel rate simulation. There is substantial underprediction of the pressure levels in the early portion of the combusting nozzle. Apparently, the heat release is too abrupt to provide reasonable agreement, and we attribute this in large part to the 1-step kinetics model. The predicted position of the thermal choke (see Fig. 12b) is in the initial portion of the diverging combustor section, at x/L = 45%, reinforces the idea that the heat release is too abrupt. However, this case is not directly comparable to the simulations with the 3-step kinetics model.

Fig. 13a shows the zero-velocity isosurfaces for the 50% fuel rate run. Note that there is again a long, slender reverse flow region that extends from the combustor upstream well into the isolator. It is quite interesting that this structure is along the opposite corner from the previous cases involving incremental inflow Mach number. This suggests that these structures are not tied to the presence of the cascade injector. It is not clear what drives the origin of this structure. Fig. 13b illustrates the crossflow streamlines and axial Mach contours, as before. There is only one major streamwise vortex in this cut plane, compared to the more coupled counter-rotating vortices seen in the previous case. It is important to note that there is no data available from the ICR tests to confirm or deny the presence of the long slender reverse flow region in the isolator.

V. Conclusions

Wind-US has been utilized to simulate the Burrows-Kurkov hydrogen-air supersonic combustion experiment. It is shown that excellent results for the location of ignition and the combustor exit flow state can be obtained provided the kinematic and thermal boundary layer prior to the test section closely resembles that in the experiment. Also, the ignition delay is moderately affected by the choice of turbulence model.

Wind-US has been successfully utilized to simulate a complex 3-D hydrocarbon-air ramjet experiment. The substitution of gaseous ethylene for superheated JP-7 gas appears to produce an appropriate heat release, based on direct comparison to experimental data for the axial pressure distribution. The thermal throat location and thrust predictions also lend confidence to the combustion portion of the flowpath prediction. Furthermore, it appears that the 3-step kinetics model results in a more gradual and realistic heat release than the 1-step model. The poor performance of the numerical isolator compared to experiment remains an open issue for future work.

VI. Acknowledgments

Funding for this work was provided by the former Space Transportation Office at NASA Glenn Research Center, under contract C-31035-T (Aerospace Corporation) and NAS3-00145 (QSS Group, Inc.), and by Arnold Engineering Development Center under contracts ATA-04-069 and ATA-05-20. The authors would like to thank Dr. Dennis Lankford (AEDC) and Dr. Shaye Yungster (OAI) for providing valuable assistance with the chemical kinetics models, and Mr. Diego Capriotti (NASA Langley) for providing ICR experimental data.

VII. References

1. Frate, F. C., Haas, M., Van Dyke, K. J., and Andreadis, D., "Computational Analyses of the Forebody, Inlet, and Isolator Flowpath for an Air-breathing, Hydrocarbon-Fueled Engine System," NASA/CR-2004-212727, April 2004.
2. Frate, F. C., "Inlet/Isolator 3D Computational Analyses for the ISTAR Flowpath," NASA/CR to be published in 2005
3. Engblom, W., "Numerical Prediction of NASP Model 5B and RBCC ISTAR Nozzle Performance Using Wind Code," NASA/CR-2003-212728, Nov. 2003.
4. Nelson, C. C., Lankford, D., and Nichols, R. H., "Recent Improvements to the Wind(-US) Code at AEDC," AIAA-2004-0527, Jan. 2004.
5. Lankford, D. W., Mani, M., "Wind Thermochemical Models and Recent Improvements," AIAA-2003-0545, Jan. 2003.
6. Lankford, D. W., Nelson, C. C., "Application of the Wind Flow Solver to Chemically Reacting Flows," AIAA-2002-0673, Jan. 2002.
7. DalBello, T., "WIND Validation Cases: Computational Study of Thermally Perfect Gases," AIAA-2004-0546, Jan. 2004.
8. Rocket Based Combined Cycle Consortium, "Injector Characterization Rig (ICR) Final Report," ISTAR 6100-03-157, prepared for NASA Marshall Space Flight Center, Dec. 2003.
9. Burrows, M. C., Kurkov, A. P., "Analytical and Experimental Study of Supersonic Combustion of Hydrogen in a Vitiated Airstream," NASA TM-X-2828, Sept. 1973.
10. Mani, M., Bush, R. H., Vogel, P. G., "Implicit Equilibrium and Finite-Rate Chemistry Models for High-Speed Flow Applications," AIAA-91-3299-CP, 1991.
11. Ebrahimi, H. B., "CFD Validation for Scramjet Combustor and Nozzle Flows, Part I," AIAA-1993-1840, June 1993.
12. Aerosoft, Inc., *GASP Version 3 User's Manual*, May 1999.
13. Evans, J. S., and Schexnayder, C. J., "Influence of Chemical Kinetics and Unmixedness on Burning in Supersonic Hydrogen Flames," AIAA Journal, Vol. 18, No. 2, 1979, pp. 805-811.
14. Jachimowski, C. J., "An Analysis of Combustion Studies in Shock Expansion Tunnels and Reflected Shock Tunnels," NASA TP-3224, July 1992.
15. Baurle, R.A. and Eklund, D.R. "Analysis of Dual-Mode Hydrocarbon Scramjet Operation at Mach 4--6.5," Journal of Propulsion & Power, Vol. 18, No. 5, 2002, pp. 990-1002.
16. Yungster, S., Suresh, A., and Stewart, M.E.M., "A Study of Ram Combustor Performance using 1D and 3D Numerical Simulations," AIAA-2005-0430, Jan. 2005.
17. Mawid, M. A., Private Communication, Engineering Research and Analysis Co, report No. ERAC.EF.5.1997,

Wright-Patterson AFB, Ohio.
18. Westbrook, C. K., Dryer, F. L., "Simplified Reaction Mechanisms for the Oxidation of Hydrocarbon Fuels in Flames," *Combustion Science and Technology*, Vol. 27, 1981, pp. 31-43.
19. Edwards, T., Maurice, L. Q., "Surrogate Mixtures to Represent Complex Aviation and Rocket Fuels," *J. of Propulsion and Power*, Vol. 17, No. 2, March-April 2001, pp. 461-466.
20. Launder, B. E., Spalding, D. B., "The Numerical Computation of Turbulent Flows," *Computer Methods in Applied Mechanics and Engineering*, Vol. 3, 1974, pp.269-289.
21. Heiser, W. H., and Pratt, D. T., *Hypersonic Airbreathing Propulsion*, AIAA Education Series, Washington, DC. 1994
22. Hoxie, S. S., Andreadis, D., and Liu, J., "A CFD Evaluation Of Injector Concepts For The ISTAR Combustor," December JANNAF Joint Meeting, 2003.

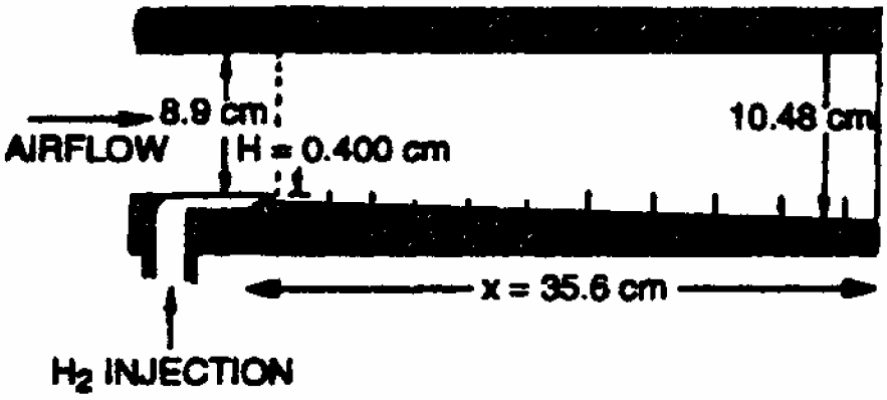

Fig. 1: Burrows-Kurkov H_2-vitiated air supersonic combustion test section geometry

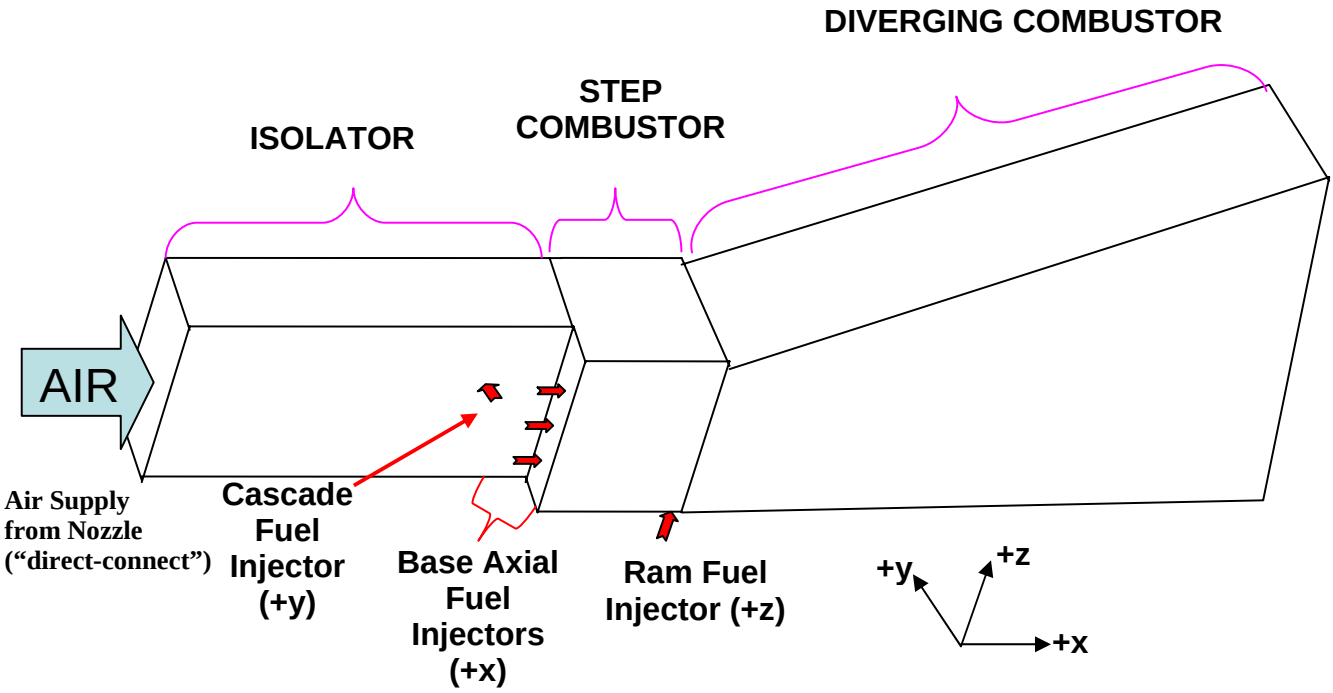

Fig. 2: Key representative ICR geometry features

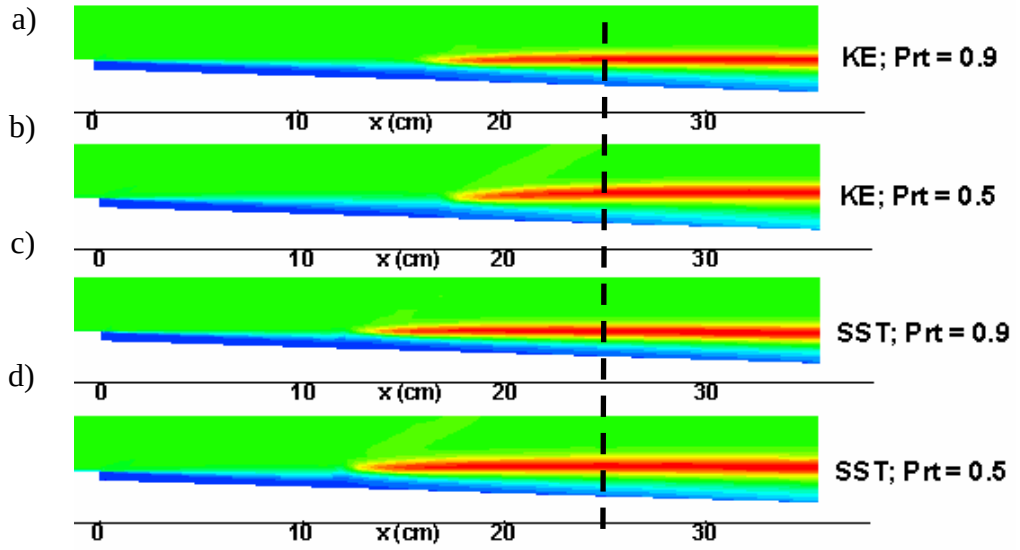

Fig. 3: Temperature contours for Burrows-Kurkov simulations with uniform upstream flow.
a) *k*-ε with Pr_t=0.9; b) *k*-ε with Pr_t=0.5; c) SST with Pr_t=0.9; d) SST with Pr_t=0.5

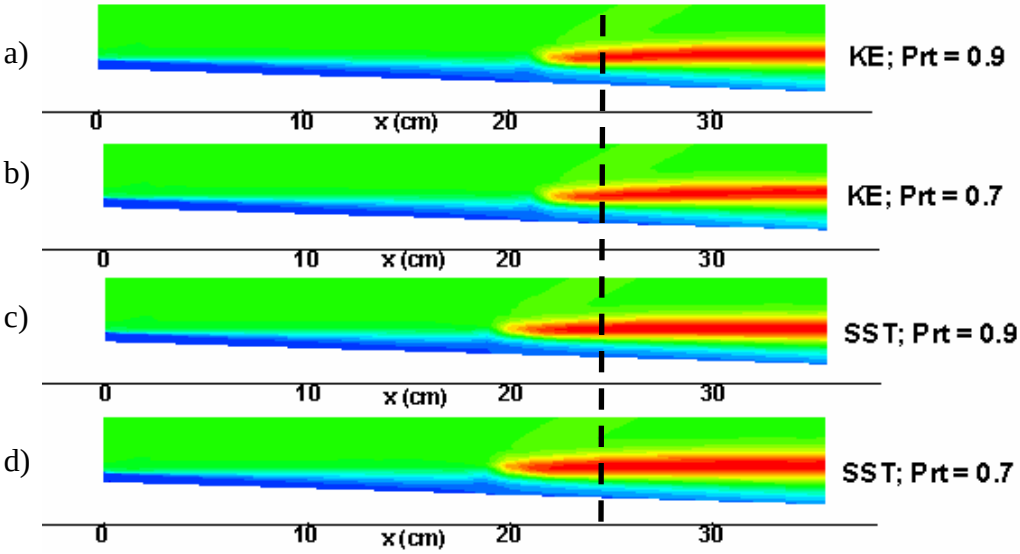

Fig. 4: Temperature contours for Burrows-Kurkov simulations with specified inflow boundary layer.
a) *k*-ε with Pr_t=0.9; b) *k*-ε with Pr_t=0.7; c) SST with Pr_t=0.9; d) SST with Pr_t=0.7

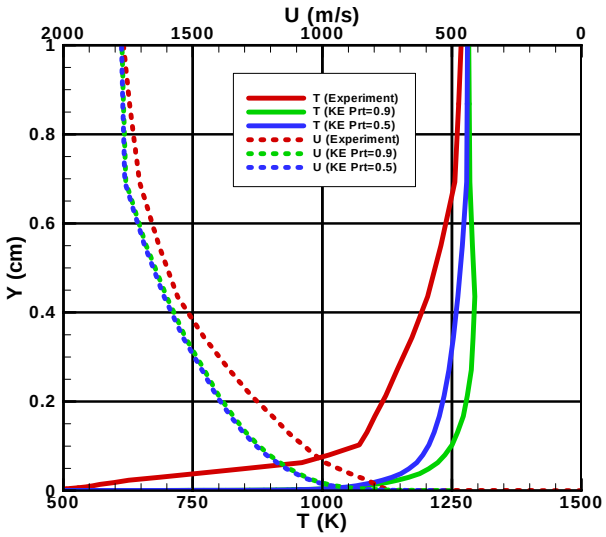

Fig. 5: Experiment and developed boundary layer profiles for Burrows-Kurkov simulations

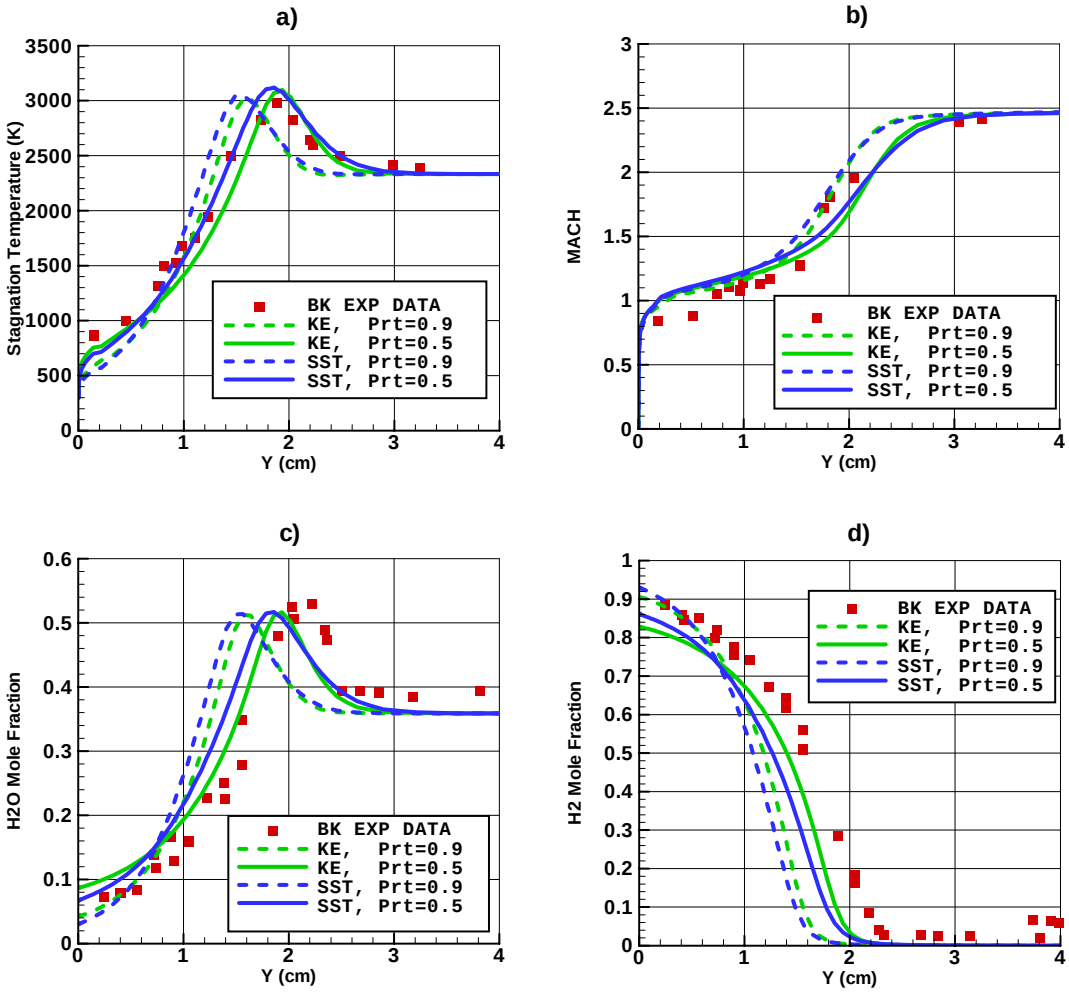

Fig. 6: Comparison of combustor exit profiles for Burrows-Kurkov simulations (Wind-US vs. experiment). a) Stagnation temperature, b) Mach number; c) H_2O mole fraction, d) H_2 mole fraction

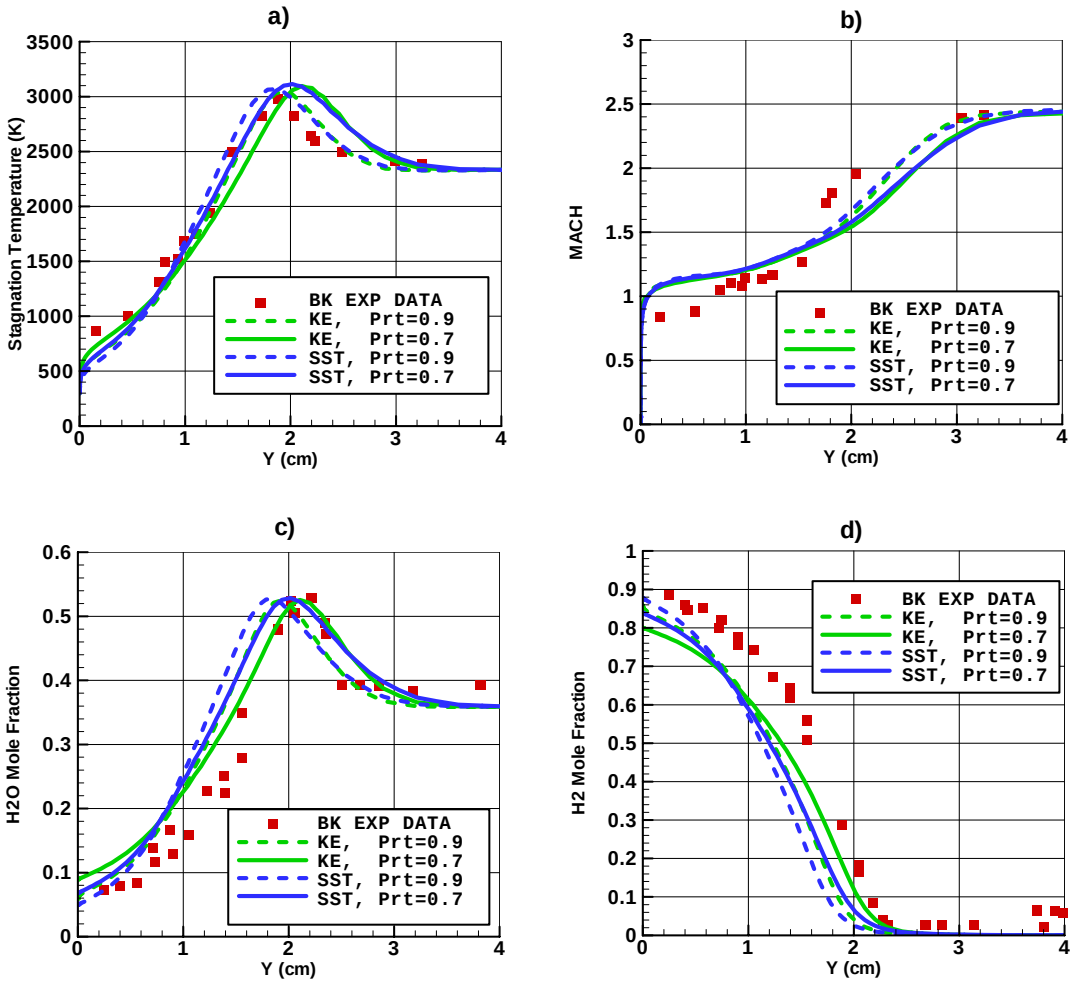

Fig. 7: Comparison of combustor exit profiles for Burrows-Kurkov simulations with specified inflow boundary (Wind-US vs. experiment). a) Stagnation temperature, b) Mach number; c) H_2O mole fraction, d) H_2 mole fraction

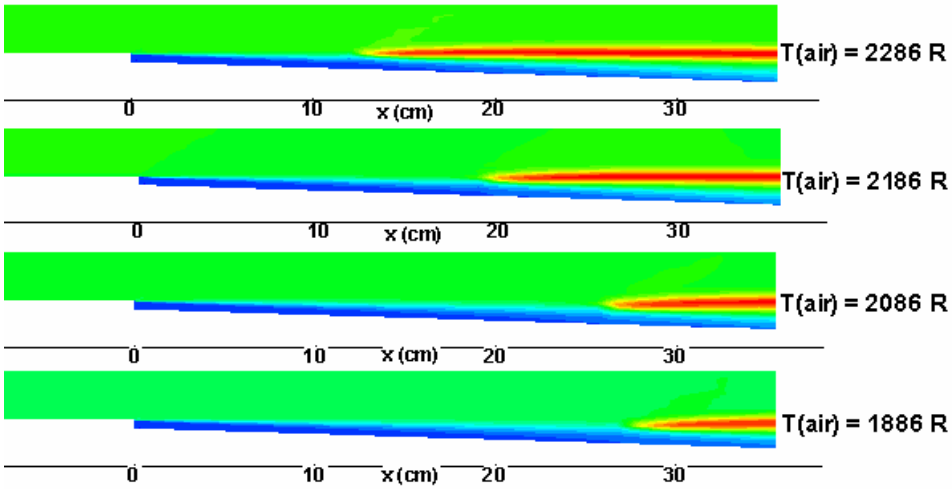

Fig 8: Sensitivity of ignition delay to vitiated air temperature

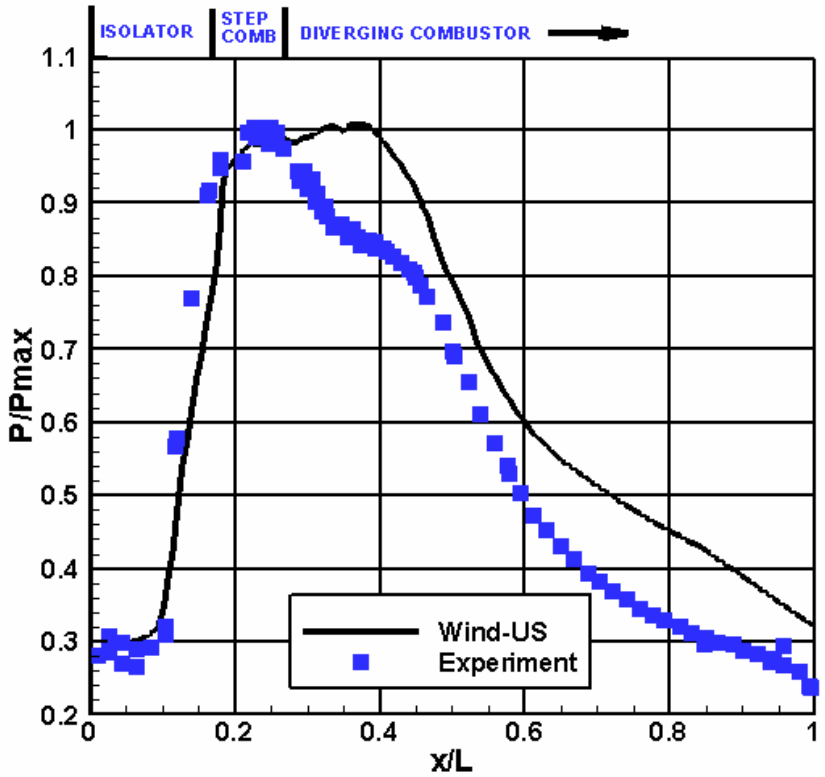

Fig. 9a: Comparison ethylene-air simulation vs. ground test data for axial pressure profiles (Mach 2.25 inflow assumed in simulation)

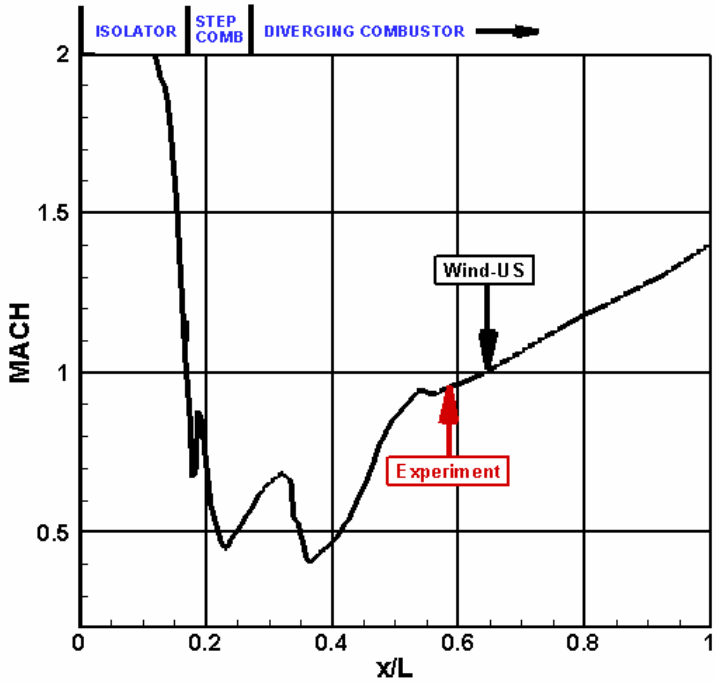

Fig. 9b: Comparison of thermal throat location for ethylene-air simulation vs. ground test data (Mach 2.25 inflow assumed in simulation)

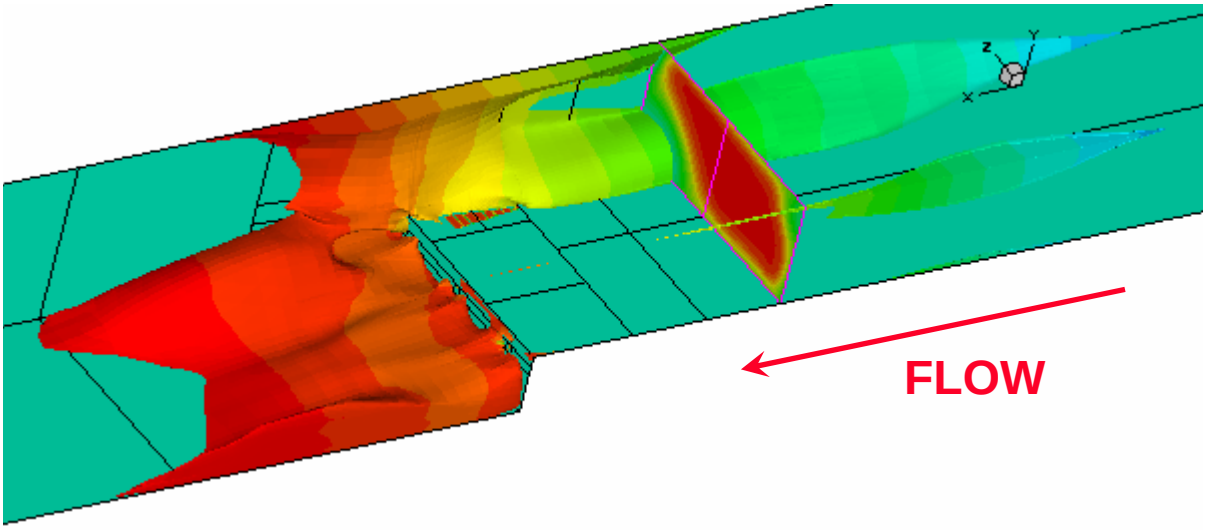

Fig. 10a: Zero *u*-velocity isosurfaces colored by pressure contours illustrated reverse flow regions
(Mach 2.25 inflow assumed in simulation; main flow is from right to left)

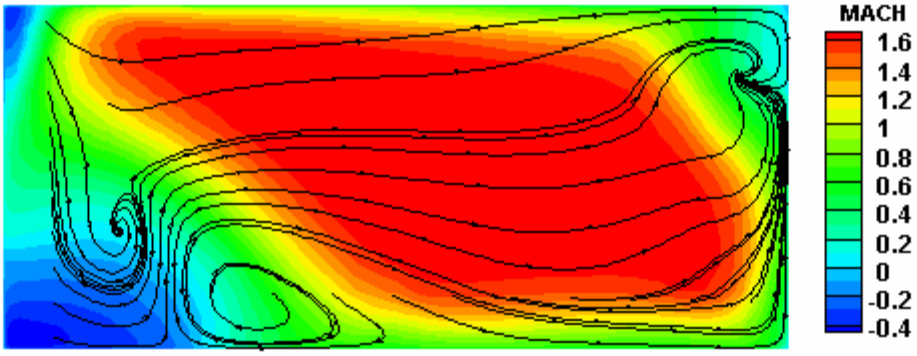

Fig. 10b: Crossflow cut with Mach (plus direction) contours plus crossflow streamlines
(Mach 2.25 inflow assumed in simulation)

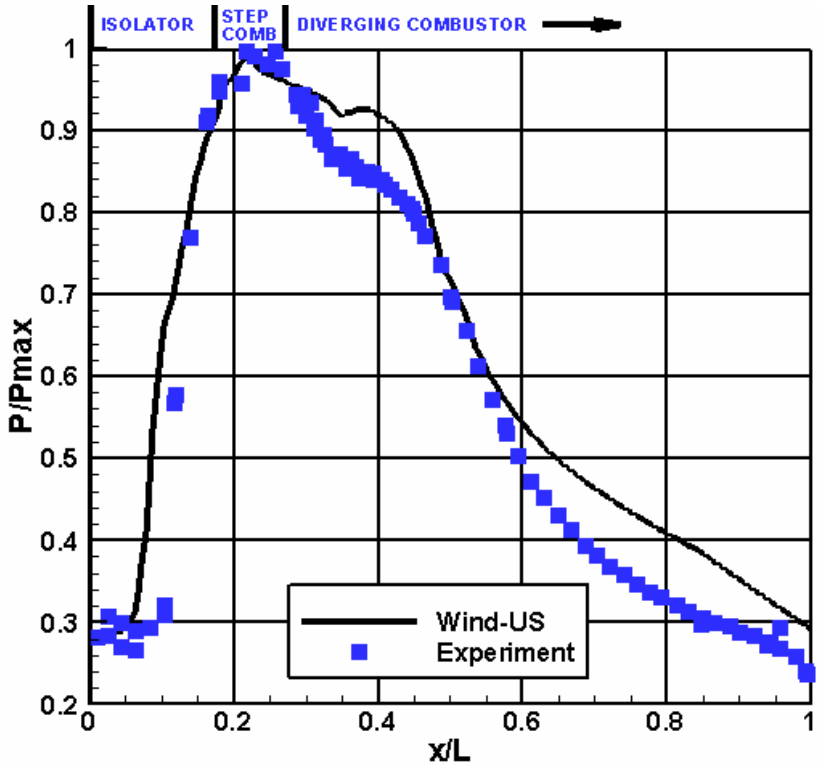

Fig. 11a: Comparison ethylene-air simulation vs. ground test data for axial pressure profiles (Mach 2.0 inflow assumed in simulation), ensemble-averaging of the last 100 realizations prior to unstart.

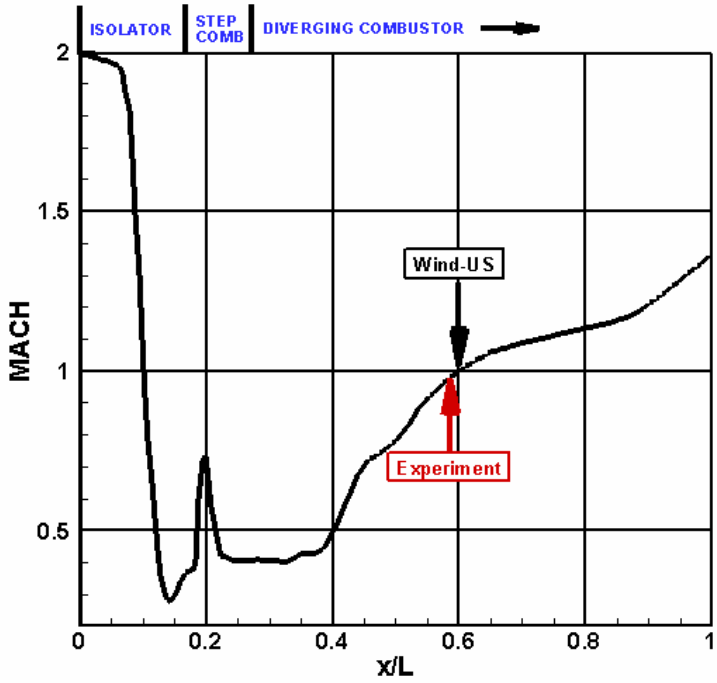

Fig. 11b: Comparison of thermal throat location for ethylene-air simulation vs. ground test data (Mach 2.0 inflow assumed in simulation), ensemble-averaging of the last 100 realizations prior to unstart

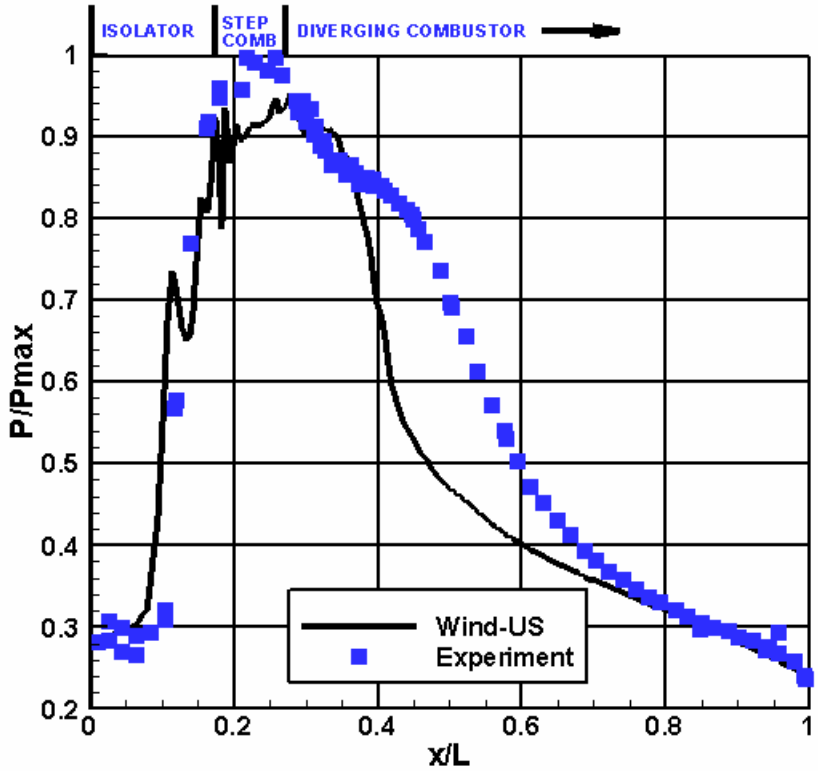

Fig. 12a: Comparison ethylene-air simulation vs. ground test data for axial pressure profiles (50% fuel rate assumed in simulation)

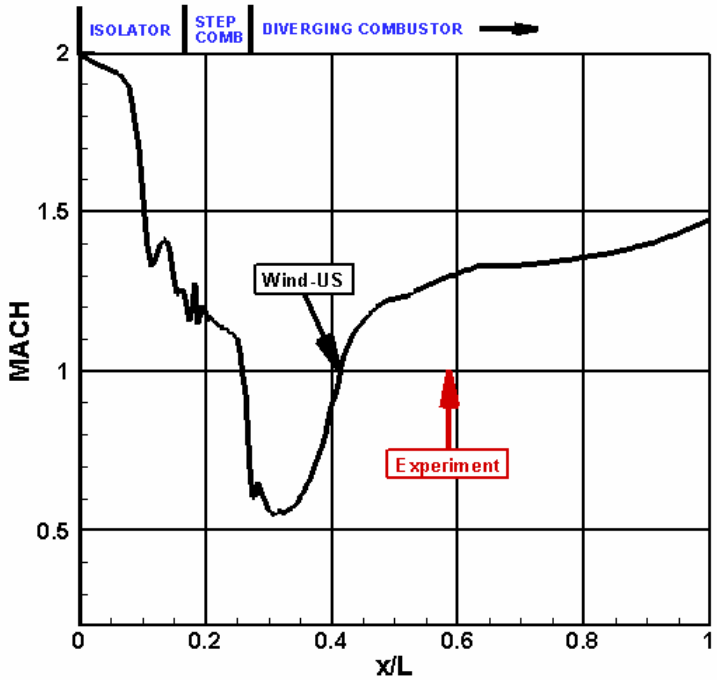

Fig. 12b: Comparison of thermal throat location for ethylene-air simulation vs. ground test data (50% fuel rate assumed in simulation)

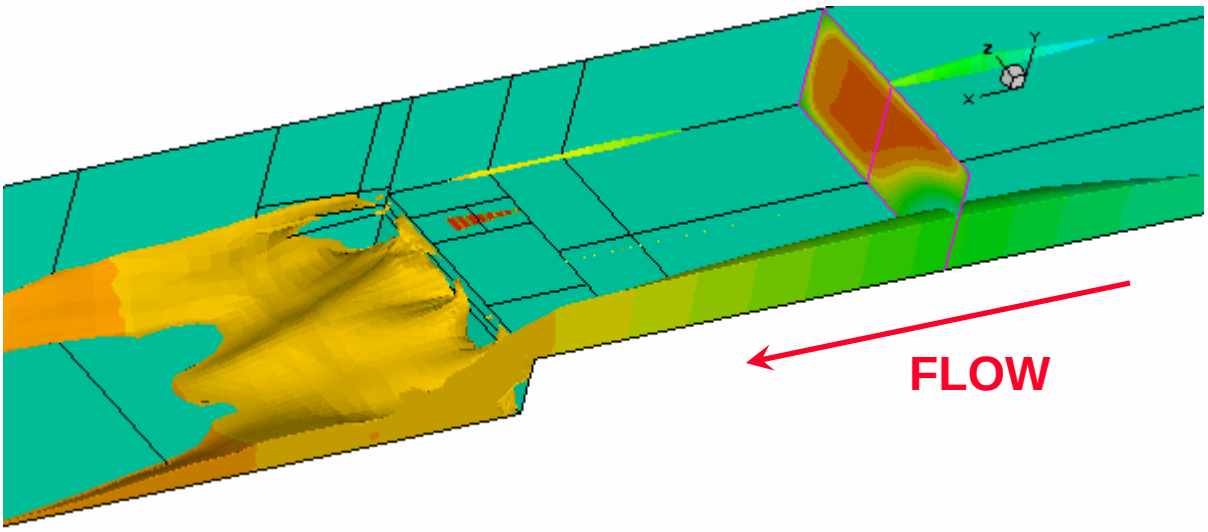

Fig. 13a: Zero *u*-velocity isosurfaces colored by pressure contours illustrated reverse flow regions, plus crossflow cut location (50% fuel rate assumed in simulation; main flow is from right to left)

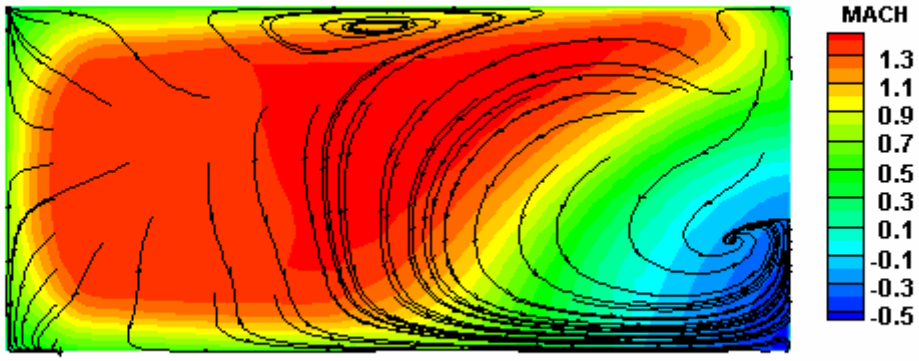

Fig. 13b: Crossflow cut with Mach (plus direction) contours plus crossflow streamlines (50% fuel rate assumed in simulation)